RAPID COMMUNICATION

Reconstruction and functionalization of aerogels by controlling mesoscopic nucleation to greatly enhance macroscopic performance

Chen-Lu Jiao(焦晨璐)[1,2], Guang-Wei Shao(邵光伟)[3], Yu-Yue Chen(陈宇岳)[2], and Xiang-Yang Liu(刘向阳)[1,†]

[1] *College of Ocean and Earth Sciences, Shenzhen Research Institute of Xiamen University, Xiamen University, Shenzhen/Xiamen* 361005, *China*
[2] *College of Textile and Clothing Engineering, Soochow University, Suzhou* 215006, *China*
[3] *Engineering Research Center of Technical Textiles, Ministry of Education, College of Textiles, Donghua University, Shanghai* 201620, *China*

(Received 13 January 2023; revised manuscript received 28 January 2023; accepted manuscript online 6 February 2023)

This work presents a strategy for the mesoscopic engineering of hierarchically structured sodium alginate (SA) aerogels to enhance the macroscopic performance. The strategy was implemented by meso-functionalizing and reorganizing SA aerogels via controlled heterogeneous nucleation, in which microcrystalline cellulose-manganese dioxide (MCC-MnO_2) nano-crystallites worked as template. Due to the short rod-like structure and abundant hydroxyl groups of MCC-MnO_2, the organized mesostructure of SA aerogels was reconstructed during the assembly of SA molecule chains, which gave rise to a significant enhancement in macroscopic performance of SA areogels. For instance, the functionalized and reconstructed MCC-MnO_2/SA aerogels acquired a more than 70% increase in mechanical strength with an excellent deformation recovery. Furthermore, an almost double enhancement of removal capacity for metal ions (i.e., Cu^{2+} and Pb^{2+}) and organic dyes (i.e., congo red and methylene blue) was obtained for MnO_2/SA aerogels, with an 87% repossession of the pollutants removal performance after 5 operation cycles.

Keywords: mesoscopic reconstruction, aerogel, sodium alginate, microcrystalline cellulose, MnO_2 nanoparticles

PACS: 81.10.Aj, 81.20.Rg **DOI:** 10.1088/1674-1056/acb912

1. Introduction

As a type of soft materials, aerogels are mesomaterials with three-dimensional (3D) open networks assembled by cohesive nanoparticles or polymer molecules. The materials have attracted increasing interest due to their light weight, high porosity and exceptional and unique physical properties. Aerogels have been applied in thermal insulation, environmental protection (adsorption, filtration and oil–water separation), tissue engineering, energy storage, sound adsorption, etc.[1–4] Regarding the performance of aerogels, their various porous structures play a crucial role in sorting guest species of different sizes and shapes. Moreover, in the applications of separation and filtration, the structural flexibility and porous regularity of aerogels are key considerations.

Conventional aerogels with 3D interpenetrating porous networks have intrinsic advantages in that their porosity allows efficient removal of environmental pollutants because of the abundant porous units.[5] Nevertheless, these aerogels present fundamental disadvantages in various applications. For instance, for high-demand and special applications, conventional aerogels with interpenetrating networks have a slow diffusion of guest species. In addition, the disordered porous structure results in a poor mechanical performance, i.e., fragility and a weak network linkage. The ability to structurally reconstruct the channels and cavities of aerogels at the mesoscale will provide new opportunities in engineering filtration media.[6–10]

In this regard, mesoscopic reconstruction induces the reassembly of aerogel skeletons and integrates additives with specific functions to achieve distinctive synergistic properties and enhance performance.[11–13]

The latest studies revealed that the performance of soft materials is directly correlated with the five factors that affect structures: (1) topology of structural networks, (2) correlation length, (3) orientation and (4) interactions of structural units, and (5) hierarchy of the mesoscopic structure.[14–16] Based on these principles, the macroscopic performance or functionality of soft materials can be modified to enhance the performance or to add certain functions, as follows. (i) Reconstruct the mesoscopic structure by altering one of the several aforementioned parameters to acquire a newly desired performance. (ii) Attach functional components, e.g., functional molecules and nanoparticles, to the self-assembled mesoscopic network structure of the soft materials to give the materials additional functions (Fig. 1A).[7,17,18]

Aerogels formed from hydrogels or molecular gels are controlled by nucleation.[14,19] Therefore, the mesostructure of aerogels can be reconstructed by controlling nucleation via the introduction of seeds.[8] This meso-reconstruction can be adopted to modify the macroscopic performance of soft materials. Here, we introduce a new strategy in mate-

†Corresponding author. E-mail: liuxy@xum.edu.cn

© 2023 Chinese Physical Society and IOP Publishing Ltd

rials science for combining meso-reconstruction and meso-functionalization. In contrast to the conventional approach illustrated by Fig. 1A(a), the seeds were first coated with functional components. Then, the coated seeds were introduced into solutions or liquids that were further processed to produce functional soft materials (Fig. 1A(b)). The functionalized seeds not only serve as functional components but also as agents for the recontruction of the mesoscopic structure of soft materials.

Sodium alginate (SA), a particularly attractive naturally created anionic polysaccharide, has been investigated extensively for its hygroscopicity, biocompatibility, biodegradability and reversibility in aqueous gelation chemistry with certain divalent cations (e.g., Ba^{2+}, Ca^{2+}, Sr^{2+}).[24–26] The various applications of SA include separating pollutants from wastewater,[27–29] serving as scaffolds for tissue engineering,[30,31] wound dressing[32,33] and drug delivery.[34,35] As an unbranched binary block copolymer, the primary structure of SA is composed of 1→4 linked β-D-mannuronic acid (M) and α-L-guluronic acid (G) residues in various proportions (Fig. 1B).[26] The ion-responsive nature of SA means that the divalent cations can cooperatively bind between the G-units of adjacent SA chains, creating ionic interchain crosslinking, which generates SA gel networks and the typical "egg-box" model.[36,37] However, neat SA aerogels display some unsatisfactory properties, i.e., low mechanical strength and hydroexpansivity.[38] Therefore, implementing the new strategy of mesoscopic reconstruction/functionalization to enhance the performance and impart new functions for SA materials is an ideal approach.

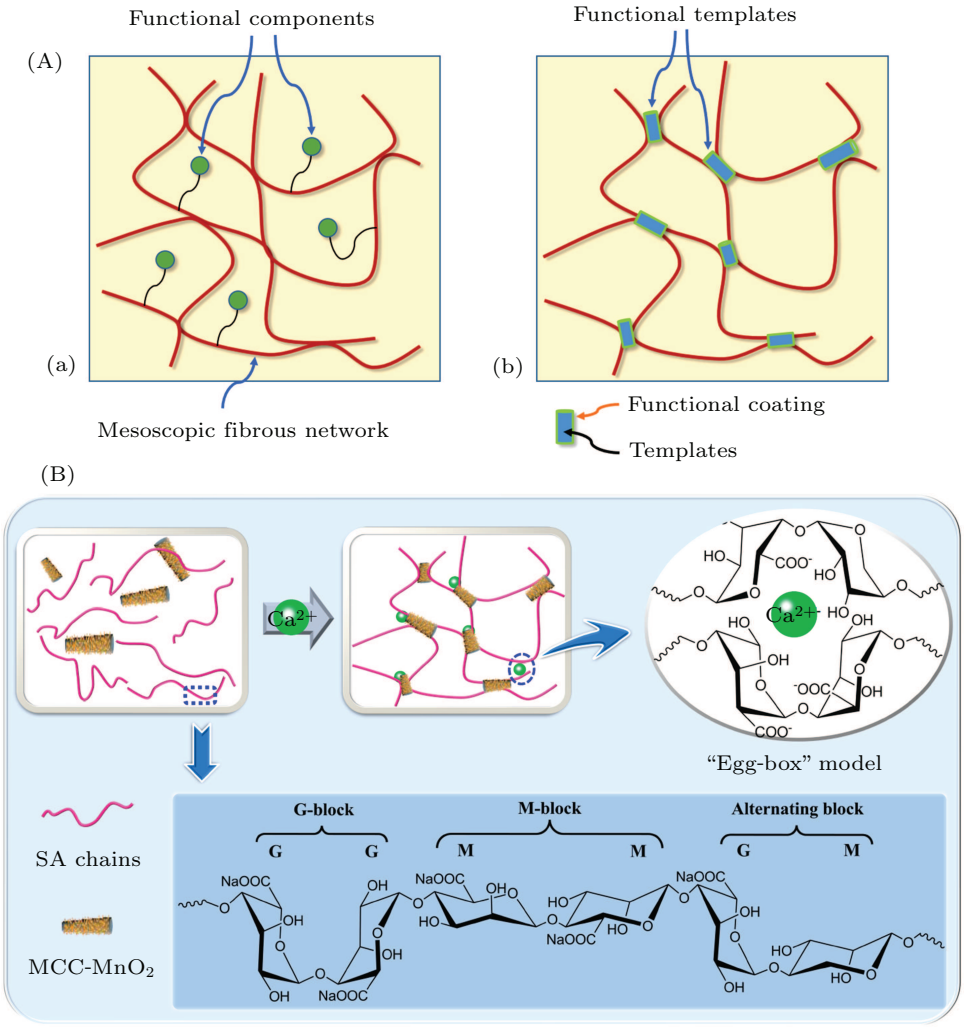


Fig. 1. (A) Schematic illustration of mesoscopic functionalization. (a) Conventional mesoscopic functionalization: the attachement of functional components (nanocomponents or molecules).[20–22] (b) Functional templating: one of the most effective ways to recontruct soft materials.[23] (B) Schematic depiction of the formation of MCC-MnO_2/SA (MMSA) aerogels and the molecular structures.

Microcrystalline cellulose (MCC) is a fine, white, odorless, highly crystalline, and naturally occurring biodegradable material that can be derived from cellulose by acid hydrolysis of cotton or wood pulp.[39] It was demonstrated that the performance enhancement of monoliths via MCC can give rise to environmentally friendly aerogels with a low density/high porosity and a remarkably improved filler function.[40,41] Thus, MCC was chosen as seeds for reengineering SA aerogels.

Figure 1A shows the routes to incorporate "functional components" into the mesoscopic structure and recon-

struct the mesoscopic network structure of soft materials.[14] MnO_2 nanoparticles can be applied as adsorbents[42,43] and catalysts,[44] etc. As highlighted in Fig. 1A(b), MnO_2-covered MCC (MCC-MnO_2) particles can further enhance the performance of SA aerogels.[7] As MCC-MnO_2 particles can influence the networks during the gelation of SA, they were adopted as functionalized templates to guide and reconstruct SA networks (as shown in Fig. 1B) to prepare aerogels. This strategy (Fig. 1A(b)) will offer an enhanced mechanical performance via the MCC particles and an improved adsorption capacity via the MnO_2 coating.

2. Results and discussion

2.1. Principles of meso-functionalization and reconstruction of SA networks

The meso-functionalization and reconstruction of SA networks are illustrated in Fig. 2. The first step was to synthesize MCC-MnO_2 composite particles (Figs. 2(a) and 2(e)). As shown, MCC microrods served as templates to trigger the heterogeneous nucleation (or templating) of MnO_2 nanocrystals on the surfaces. In this process, Mn^{2+} and MnO_4^- were precursors of MnO_2 nanoparticles via the redox method.[45] According to previous researches, cellulose gelation was controlled by nucleation, leading to the formation of polymeric networks.[46,47] Thus, the MCC-MnO_2 composite particles served as functionalized templates to trigger SA network formation/gelation to form MCC-MnO_2/SA (MMSA) gels. Note that the above process is synergistic, and incorporating MCC-MnO_2 with SA chains can avoid aggregation and optimize the dispersion of MnO_2 nanoparticles.

From a rheological perspective, a major challenge in formulating MMSA aerogels is to predict the effect of MCC-MnO_2 on the overall assembly behaviors and performances of the composites. Therefore, neat SA aerogels and hybrid MMSA aerogels were prepared with a similar procedure for comparison. These MMSA hybrids were named MMSA-x on the basis of the weight ratios, x, of MCC-MnO_2, and they can be readily molded to any shape (e.g., monoliths, films, fibers) according to the application. For more details, see Appendix A.

As mentioned above, the macroscopic property can be regulated by the five factors influencing mesoscopic structure.[14] The correlation length ξ_1 is defined as the average mesh size of the network. Compared with the neat SA aerogel, the mesoscopic network unit of the MMSA aerogel changed as the correlation length (ξ_2) decreased, as shown in Figs. 2(b) and 2(c). Additionally, MCC-MnO_2 particles are nucleation seeds of heterogeneous nucleation, which causes a decrease in the nucleation barrier ($\Delta G^*_{heter} \leq \Delta G^*_{homo}$), as displayed in Fig. 2(d).[48–50]

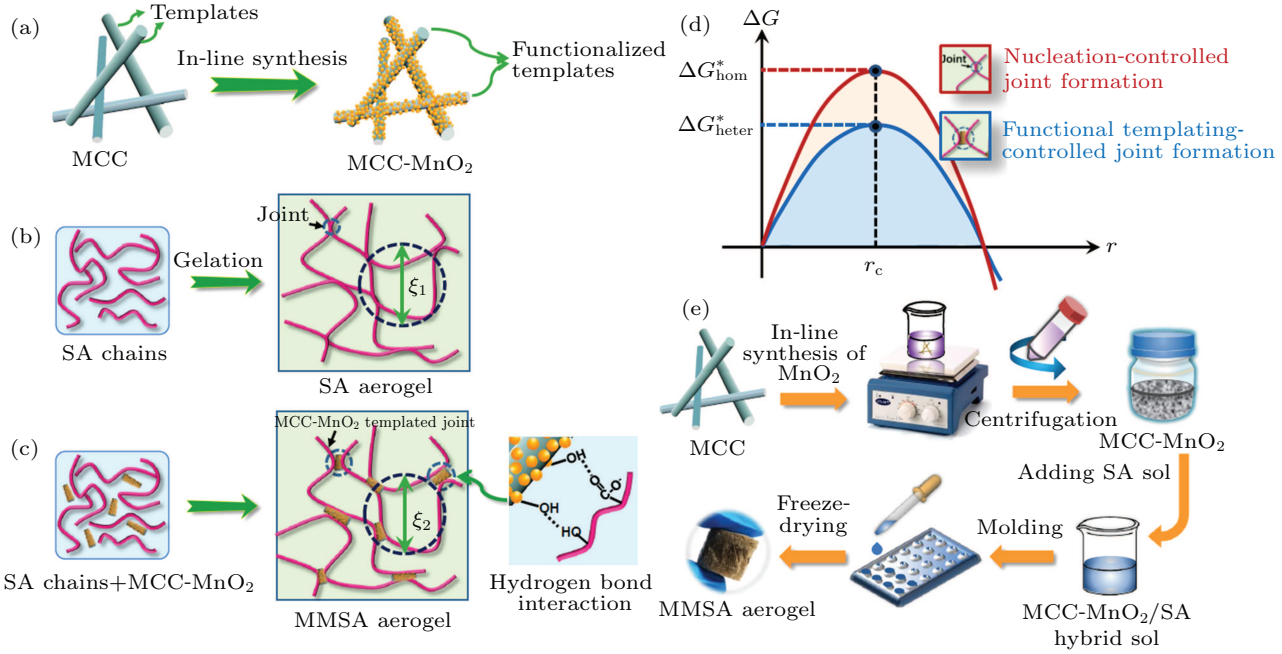


Fig. 2. The strategy of meso-functionalization and reconstruction of SA networks. (a) The in-line synthesis of MnO_2 on MCC templates, (b) physical gel and network of the neat SA aerogel, (c) network reconstruction of the MMSA aerogel templated by MCC-MnO_2, (d) illustration of nucleation-controlled gelation, (e) schematic illustration of the preparation process of MMSA aerogels.

2.2. Characterization of MCC-MnO_2 functional templates

Significant modifications of the surface morphology of MCC after coating with MnO_2 nanoparticles were observed through scanning electron microscopy (SEM) and transmission electron microscopy (TEM) photos. As displayed in Fig. 3, the MCC (Figs. 3A(a) and 3A(b)) has a smooth texture and the characteristic cellular structure of cellulose. Due to the constrained heterogeneous nucleation, these MnO_2 nanoparti-

cles disperse uniformly on the MCC surfaces are spherulites with sizes of 120–350 nm (Figs. 3A(c) and 3A(d)). Additionally, the TEM images reveal that the MnO_2 nanospheres possess spherulitic patterns composed of numerous lamella crystallites (Figs. 3A(e) and 3A(f)), which provides a large specific surface area, enabling more effective mass transport and active site accessibility.[51]

Figure 3B(a) shows the Fourier transform infrared (FTIR) spectra of MCC and MCC-MnO_2. The IR spectra in the 1500–800 cm^{-1} region (Fig. 3B(b)) characterizes the polymorphs of highly crystalline cellulose.[45] The absorption bands at 1430 cm^{-1} and 899 cm^{-1} can be ascribed to the strong CH_2 scissoring motion and the weak C–O–C stretching vibration at the β-(1→4)-glycosidic linkage, respectively. The features of these two bands are typical of cellulose I crystals. The absence of changes in the IR bands at 1430 cm^{-1} and 899 cm^{-1} indicates that the MCC in MCC-MnO_2 did not undergo any chemical modifications. Furthermore, the IR spectra of MnO_2 at 524 cm^{-1} arises from the stretching vibration of Mn–O bond in layered birnessite.[52]

In addition to FTIR, x-ray diffraction (XRD) was also employed to investigate the crystallinity of MCC-MnO_2. As displayed in Fig. 3B(c), a primary (002) lattice plane peak and a secondary overlapping of the (101) and (10$\bar{1}$) peaks were observed at the 2θ values of 22.64°, 14.96° and 16.56°, respectively, in the MCC spectrum, which indicated a typical cellulose I structure. The intense diffraction peaks at the 2θ values of 12.60°, 24.64°, 36.45°, and 65.70° should be assigned to the characteristic peaks of birnessite MnO_2.[53] However, almost no visible diffraction peaks corresponding to MnO_2 were observed in the spectrum of MCC-MnO_2, which may be ascribed to the strong diffraction peaks of MCC and the weak diffraction peaks of MnO_2 nanoparticles.

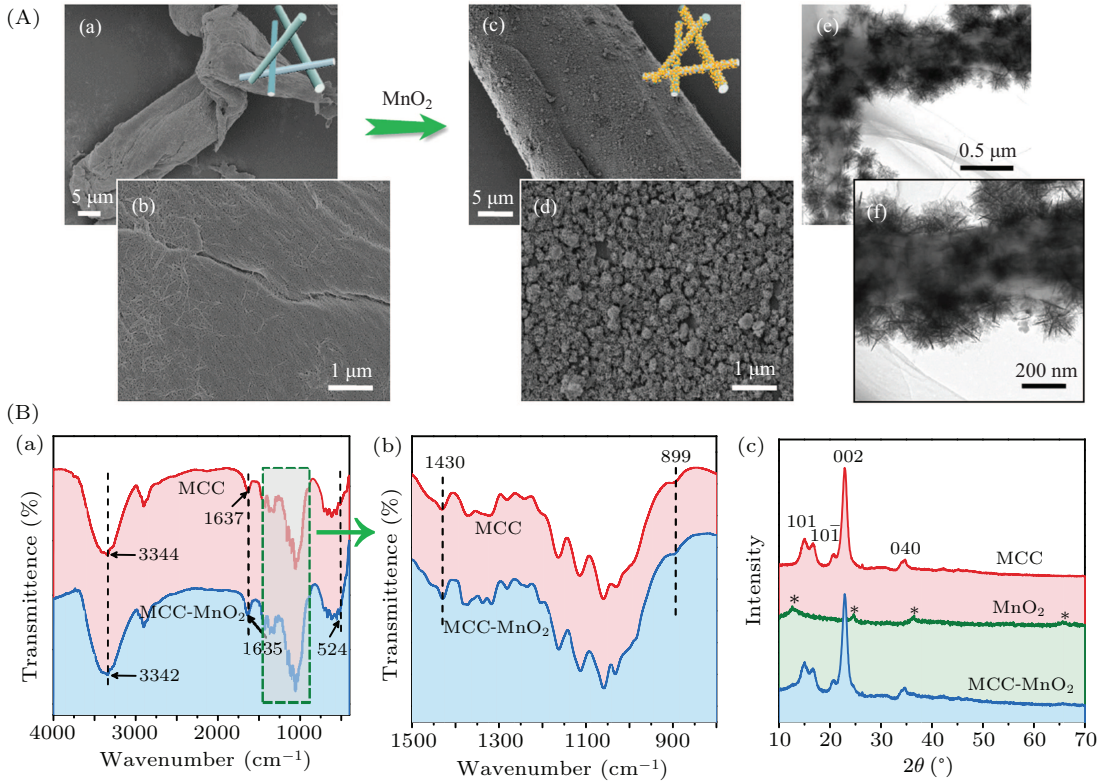


Fig. 3. (A) Microstructures of MCC and MCC-MnO_2 particles. (a), (b) SEM photos of MCC; (c), (d) SEM photos of MCC-MnO_2; (e), (f) typical TEM images of MCC-MnO_2. (B) Chemical construction and crystal structure of MCC-MnO_2: (a) FTIR spectra of MCC and MCC-MnO_2; (b) local magnified FTIR spectra of MCC and MCC-MnO_2; (c) XRD spectra of MCC, MnO_2 nanoparticles and MCC-MnO_2 particles.

2.3. Meso-reconstruction of aerogels to regulate the mesostructure

Since the viscoelastic property is determined directly by the hierarchical mesoscopic structure, representing one of the most important structural-directing macroscopic properties of gels, the gelation kinetics and rheological evolution of MMSA hydrogels were monitored. Figure 4B(a) shows the time sweep of storage modulus G' and loss modulus G'' for the MMSA-30 hydrogel immediately obtained after homogeneously blending the components. During the first 30 min (approximately), the hybrid solution appears to be a viscoelastic fluid displaying sol-like behavior. The gelation point of the solutions (t_g) is defined as the time needed to reach the inflection point on the storage modulus–time curve. G' increases gradually prior to the gelation point followed by a rapid increase of several orders of magnitude, and then it levels off after approximately 2 h when G' and G'' become stable. These characteristics enable a direct relation between the gelation process and time, which is highly consistent with the G'–time curve.

To explore how the MCC-MnO_2 particles influence t_g and

viscoelasticity, the evolution of the storage modulus G' of a 1.5% (w/v) SA solution with the MCC-MnO_2 fractions was examined and is shown in Fig. 4B(b). After an induction time t_g, G' of all the samples experienced a sharp increase, indicating the formation of mesoscopic networks of SA.[14] Furthermore, t_g decreased gradually with the added quantity of MCC-MnO_2 templates, implying that the formation of the mesoscopic network was promoted by MCC-MnO_2. As more MCC-MnO_2 was added, formation of much denser SA networks was promoted (Fig. 4A). Then, the SA aerogel networks showed a decreasing correlation length ($\xi_2 < \xi_1$). As a consequence, the G' of SA was enhanced by approximately one order of magnitude as the content of MCC-MnO_2 increased from 0% to 30%.

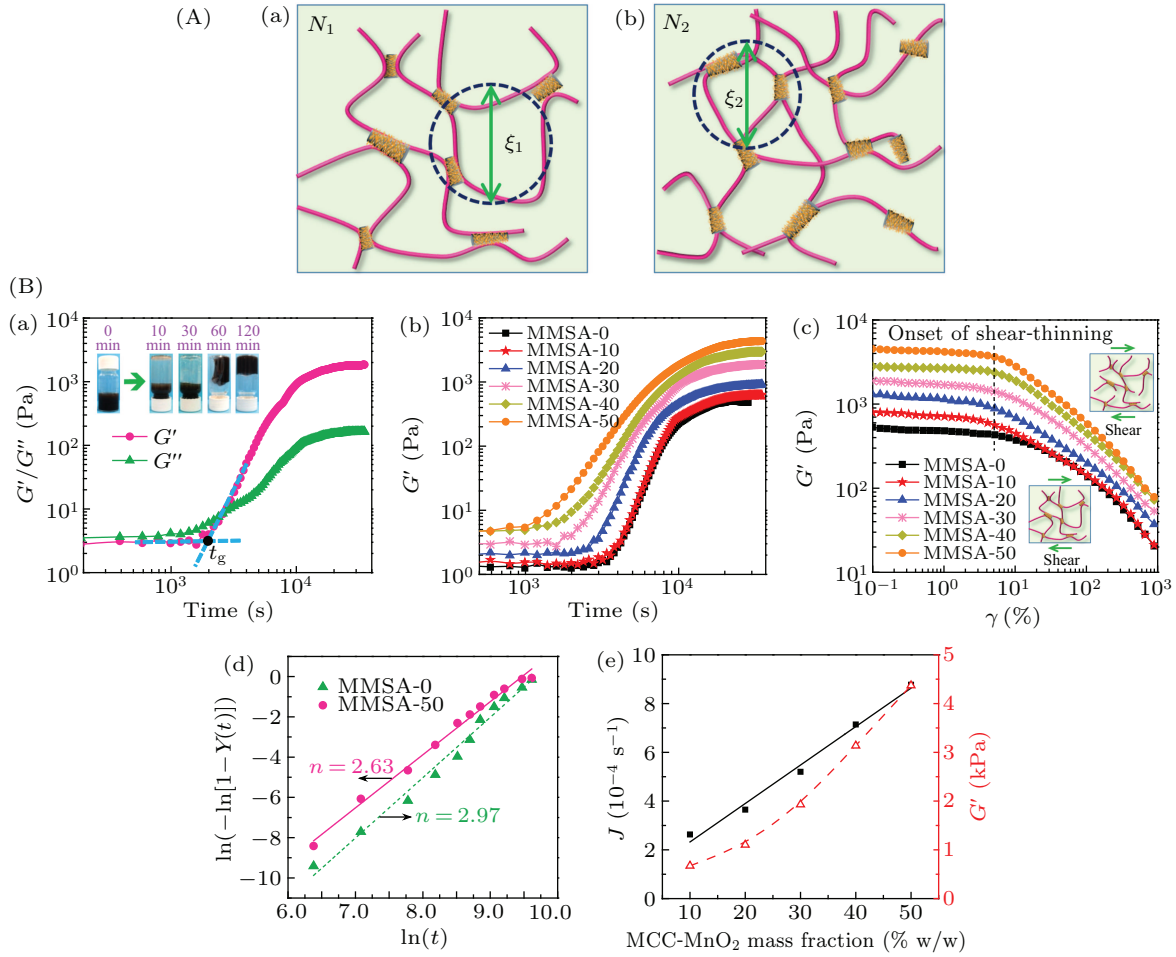


Fig. 4. (A) Effect of the MCC-MnO_2 density on the correlation length of the gel network unit. The correlation length with a (a) low and (b) high density of MCC-MnO_2, respectively. (B) Rheological behaviors of MMSA aerogels. (a) Storage modulus (G', circles) and loss modulus (G'', triangles) as a function of time sweep for the gelation of the MMSA-30 hydrogel. (b) Rheological evolution of the MMSA hybrid sols with various MCC-MnO_2 proportions. (c) G' as a function of strain sweep with a constant frequency of 1 Hz, indicating the shear-thinning behavior. (d) Dependence of ln(–ln[1–$Y(t)$]) on ln(t) based on the time-dependent rheological property G' of MMSA-0 and MMSA-50 gels. (e) Dependence of the heterogeneous nucleation rate J (closed square) and G' (open triangle) on the mass fraction of MCC-MnO_2.

To examine the kinetics of SA gelation, the Avrami equation was applied to examine the gelation process.[54] If the equation can be applied, then the process can be regarded as nucleation-controlled gelation.[55–57] At a given temperature and concentration,

$$\ln(-\ln[1-Y(t)]) = \ln K + n\ln(t), \tag{1}$$

where $Y(t)$ is the fraction of SA, which can be obtained from the following equation:

$$Y(t) = \frac{G'(t) - G'_o}{G'(\max) - G'_o}, \tag{2}$$

where $G'(\max)$ is the maximal G' at $t \to \infty$, and $G'(t)$ and G'_o denote the G' at time t and the beginning, respectively.

According to Eqs. (1) and (2), $\ln(-\ln[1-Y(t)])$ is linearly correlated with $\ln(t)$ with slopes $n = 2.97$ and 2.63 for the MMSA-0 and MMSA-50 aerogels, respectively (Fig. 4B(d)). This result implies that the gelation of SA is governed by 3D continuous nucleation, similar to other physical gels.[58] Heterogeneous nucleation can be promoted by suppressing the nucleation barrier ($\Delta G^*_{heter} \leq \Delta G^*_{homo}$ in Fig. 2A(d)) when introducing nucleation seeds (MCC-MnO_2 particles).[48–50] To examine the impact of the seeds on SA nucleation, MCC-MnO_2 composite particles were introduced as seeds into fresh SA solutions. Figure 4B(e) reveals that the introduction of these seeds leads to a shorter t_g ($J \sim 1/t_g$). According to heterogeneous nucleation theories,[48] the het-

erogeneous nucleation rate, J, can be correlated to the amount of seeds added,

$$J \sim KN^{\mathrm{o}} \exp\left[-\frac{\Delta G^*}{kT}\right]. \tag{3}$$

Here, K is the kinetic parameter, N^{o} denotes the density of seeds, k is the Boltzmann constant, and T is the absolute temperature.[50]

In the experiments, if the seed type and other conditions remain the same, then the nucleation rate J should be directly proportional to the seed density N^{o}, as confirmed by Fig. 4B(e).

Two factors influence the strength of gels. One factor is the arrangement of the rod-like MCC-MnO_2 particles in the gels. In this case, an increase in MCC-MnO_2 particles reduces the correlation length, which stiffens the SA gel networks.[59,60] The other factor is the binding strength. The hydroxyl groups of MCC-MnO_2 particles facilitate strong interactions with SA molecules (Fig. 2A(c)),[61] which synergistically enhance the strength of the gel networks.

The results of the oscillatory shear tests on the MMSA hydrogels are shown in Fig. 4B(c), where G' is plotted against strain (γ). In all cases, a linear viscoelastic regime and an apparent yield above the deformation amplitude (approximately 5%) are observed. This result corresponds to the so-called "shear-thinning" caused by the shear destruction of gel networks. G' is reduced by 3 orders of magnitude for the gels with a high density of MCC-MnO_2 (MMSA-50) and 2 orders of magnitude for the gels with a low density of MCC-MnO_2 (MMSA-0) over a strain range of 0.1%–1000%.

The 3D aerogels are applicable in many areas, i.e., cell culture, tissue engineering, pollutant adsorption, and sound insulation. Thus, the 3D porous structure of aerogels is particularly important. To determine the effect of MCC-MnO_2 particles on the gel microstructure, the mesoscopic porous structure of aerogels modified by various amounts of MCC-MnO_2 particles was examined and is shown in Fig. 5. The average pore size of MMSA aerogels decreases from 165 μm to 120 μm with increasing amounts of MCC-MnO_2 particles, and aerogels with much smaller pore sizes are obtained, which corresponds to a shorter correlation length (ξ in Fig. 2(c)).

Compared with the 3D interpenetrating crosslinked network of neat SA aerogels, the porous structures of reconstructed MMSA aerogels are more orderly and regular. The rigid and rod-like MCC-MnO_2 particles guided the soft and flexible SA chains to organize in a more orderly direction, forming more regular continuous networks and more compact and cohesive porous channels. However, when too many MCC-MnO_2 particles were added, the channels appeared to collapse and were even accompanied by a random layout (MMSA-50). This result may be due to the fact that a given quantity of SA molecules cannot accomodate an excess amount of MCC-MnO_2 particles, resulting in aggregation of the particles and the weak interactions among unaggregated MCC-MnO_2 particles. This process can be visualized in Fig. 5, where granular structures of MnO_2 nanoparticles on the MCC surface are shown in the lower right inset of the MMSA-40 aerogel.

Isometric aerogels developed an increasingly hard texture when more MCC-MnO_2 particles were incorporated. In the case of MMSA gels, the correlation length ξ decreased gradually, while the storage modulus G' increased constantly with increasing MCC-MnO_2 content according to a power law of the storage modulus G' versus ξ: $G' = \xi^{-p}$ (p: network-dependent constant)[62] (Fig. 6).

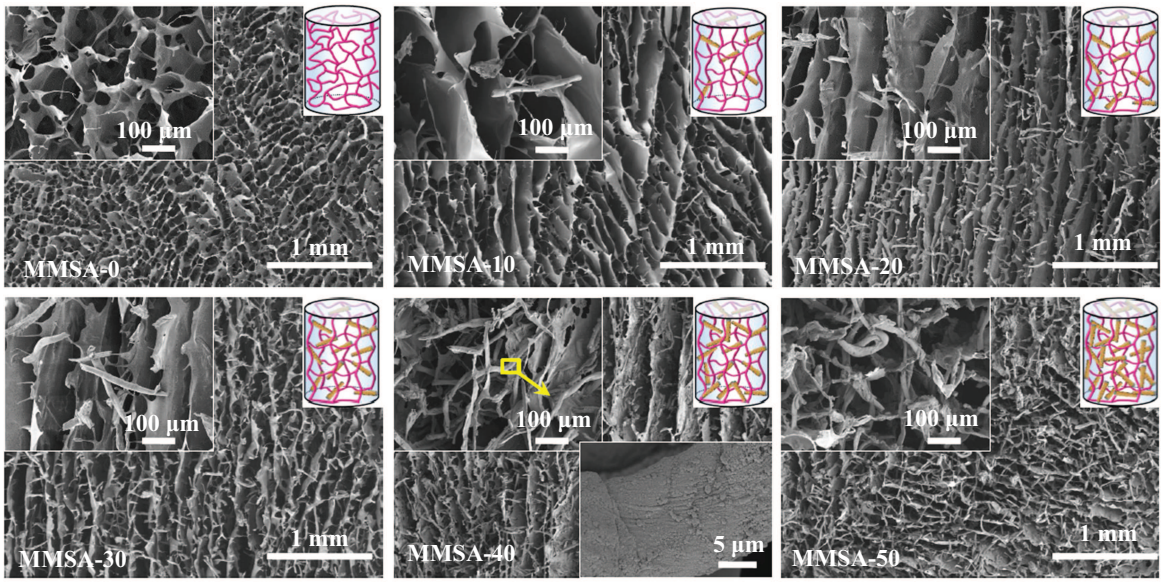


Fig. 5. SEM images of MMSA aerogels with various amounts of MCC-MnO_2 particles.

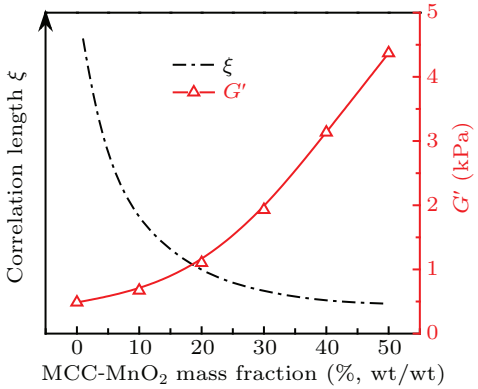


Fig. 6. Dependence of the correlation length ξ and the storage modulus G' of MMSA hybrid aerogels on the mass fraction of MCC-MnO_2.

2.4. Tuning of the mechanical properties by meso-reconstruction

As shown in Fig. 4B(e), as the nucleation rate increases, the elastic modulus G' of the SA hydrogels also increases, which substantiates the mesoscopic engineering principle that controlling the formation of soft materials to control the mesostructure allows manipulation of the material performance.

To improve the strength of SA-based aerogels and extend the application fields, MCC-MnO_2 particles were selected as functionalized templates to reconstruct SA gel networks. The as-prepared hybrid aerogels exhibited enhanced strength and G'.

The effect of MCC-MnO_2 on hybrid aerogels is strongly reflected in the mechanical properties of the hybrid MMSA aerogels. Cylindrical samples were subjected to uniaxial compression testing, and the stress–strain (σ_{gel} versus ε) curves at $\varepsilon = 60\%$ are shown in Figs. 7(a) and 7(e). Two distinct stages can be observed during the loading process: a linear-elastic region at $\varepsilon < 20\%$ followed by a densification region, and these stages were ascribed to the pore elements and network frameworks bearing the load, respectively. As shown in Table 1, the compressive strength and moduli extracted from the linear part of the stress–strain curves increase steadily with the MCC-MnO_2 loading to peak values of 315 kPa and 360.4 kPa, respectively, for MMSA-50 aerogels, representing a 71.5% increase in strength over neat SA aerogels. This increasing trend is consistent with the variation law of the storage modulus G'. As the content of MCC-MnO_2 increases, the particles share the load synergistically with the SA porous network, thus continually increasing the compressive strength.

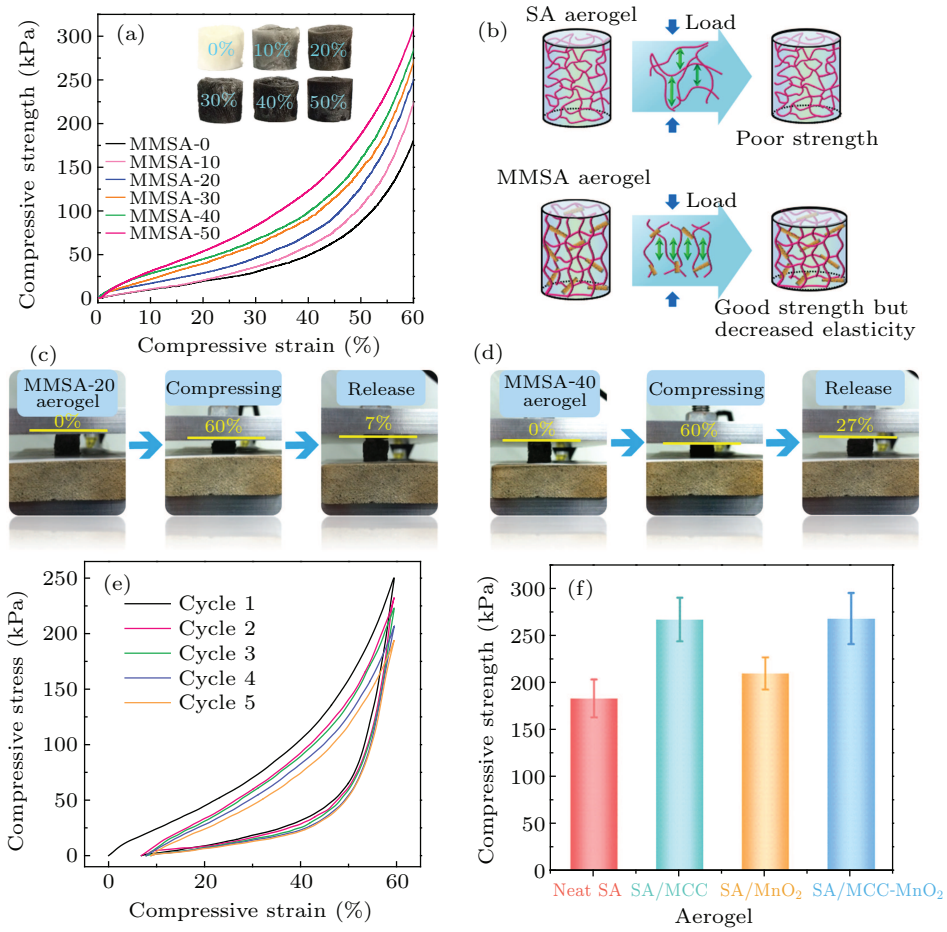


Fig. 7. Mechanical properties of hybrid MMSA aerogels. (a) Typical compressive stress–strain curves of MMSA aerogels with various MCC-MnO_2 contents. (b) Possible compressive mechanism of aerogels with different MCC-MnO_2 proportions, suggesting that MCC-MnO_2 improves the load-bearing ability. (c) Sequential photographs of an MMSA-20 aerogel during the compression process, illustrating its excellent ability to recover its structure. (d) Sequential photographs of an MMSA-40 aerogel during the compression process, indicating that the deformation recovery is slightly weakened by MCC-MnO_2. (e) Cyclic stress–strain curves of the MMSA-20 aerogel at $\varepsilon = 60\%$, showing a permanent deformation of 9.7% after 5 cycles. (f) The strength comparison of SA-based aerogels with equivalent amounts of MCC/MnO_2/MCC-MnO_2.

Table 1. Compressive strength and modulus of MMSA aerogels with various MCC-MnO_2 contents.

Aerogels	Compressive strength (kPa)	Compressive modulus (kPa)
MMSA-0	183.7	114.6
MMSA-10	227.7	120.1
MMSA-20	256.1	205.7
MMSA-30	277.4	262.3
MMSA-40	289	338
MMSA-50	315	360.4

The reinforcement mechanism of MCC-MnO_2 in SA gels is illustrated in Fig. 7(b). As indicated by Figs. 7(e) and 7(f), a significant improvement in the mechanical properties was observed when rod-like MCC-MnO_2 particles were incorporated into SA areogels. The rod-like MCC-MnO_2 particles served as nucleation seeds and important reinforcement joints in SA chain networks.

As shown in Figs. 7(c) and 7(d), the elasticity of MMSA aerogels increases as more MCC-MnO_2 particles were incorporated. However, the yield point decreases with an increase in MCC-MnO_2 particles. An MMSA-20 aerogel can spring back to 93% of its original thickness after the first compression cycle upon releasing from a 60% compressive strain, while an MMSA-40 aerogel can only recover to 73%, leading to a 27% permanent loss of its thickness. This result suggests that the deformation recovery of MMSA aerogels is slightly reduced after introducing MCC-MnO_2. Compared with flexible load-bearing SA molecular chains, rod-like MCC-MnO_2 particles serve as rigid load-bearing units, and they can support a much larger load without bearing much distortion. In contrast, the SA molecular chains are flexible, and the weak interchain interactions allow them to be compressed and restored. Therefore, the compressive strength and modulus increase gradually, while the recovery rate and yield point are reduced when more rod-like MCC-MnO_2 particles were incorporated.

Figure 7(e) shows the cyclic compression test results of an MMSA-20 aerogel. After 5 compression cycles, a reduction of approximately 9.3% of thickness was observed, but the gel could still support a 200 kPa load. This ability is sufficient for sustainable applications, such as adsorption, catalysis and capacitor equipment. To investigate the main structural components for improving the elastic modulus of SA areogels, a strength comparison of SA-based aerogels with equivalent amounts of MCC/MnO_2/MCC-MnO_2 is shown in Fig. 7(f). Evidently, the main structuralreinforced component can be derived from the rod-like MCC.

2.5. Enhancement of pollutants removal capability by meso-functionalization and reconstruction

Based on the information in the above section, the macroscopic performance of soft materials can be tuned by meso-functionalization and reconstruction. These composites of different forms (e.g., films, hydrogels and aerogels) are applicable in various fields, such as adsorption, catalysis and capacitor equipment.

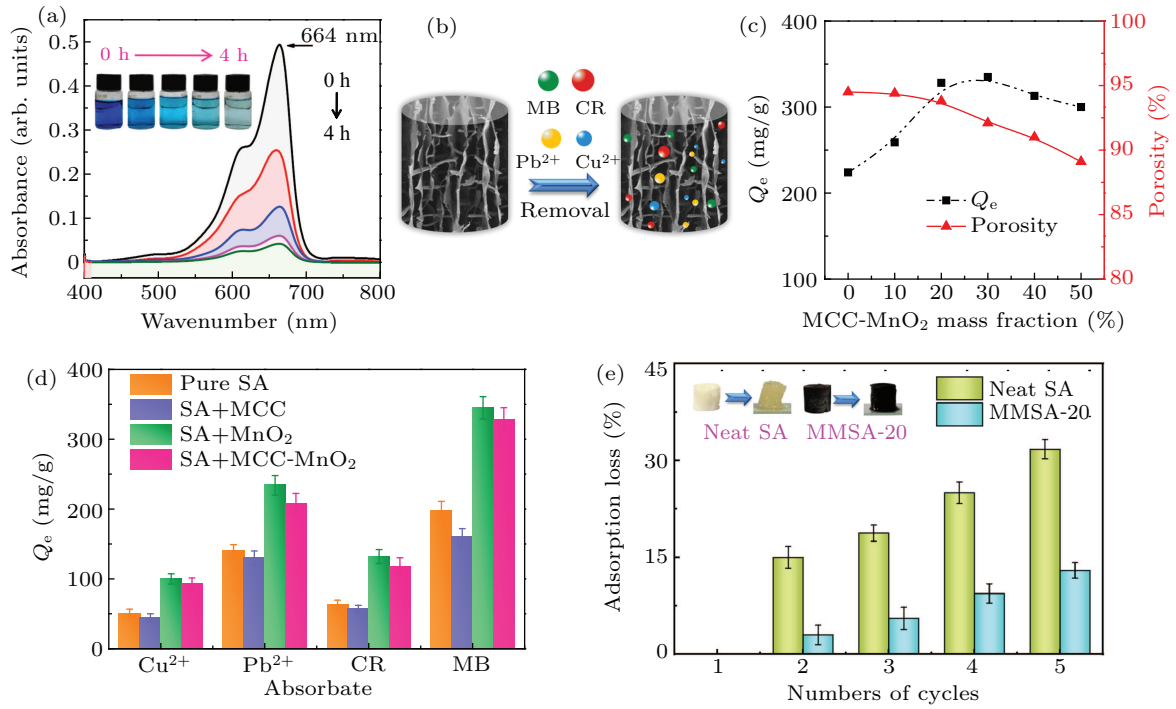


Fig. 8. (a) Absorption spectra of the MB solution in the presence of an MMSA-20 aerogel at different time intervals of 0 h, 1 h, 2 h, 3 h and 4 h. The insets are photos of the MB solution at different adsorption intervals. (b) Schematic diagram of the adsorption of MB, CR, Cu^{2+} and Pb^{2+} by the MMSA aerogel. (c) Dependence of the equilibrium adsorption capacity (Q_e) of MB and the porosity on the MCC-MnO_2 mass fraction. (d) Comparative adsorption performance of SA-based aerogels with equivalent amounts of MCC/MnO_2/MCC-MnO_2. (e) Regeneration evaluation of neat SA and MMSA-20 aerogels after MB adsorption.

To examine the enhancement of macroscopic performance of meso-functionalized and reconstructed SA aerogels, the adsorption capability for various pollutants was tested. The adsorption spectra of methylene blue (MB) solution at different intervals in the presence of an MMSA-20 aerogel are shown in Fig. 8(a). The equilibrium adsorption capacity (Q_e) for MB reaches 328.1 mg/g within 4 h, which is comparable to the adsorbability of graphene aerogels.[63] During the adsorption process, the porous channels in MMSA aerogels had a plenty of space to accommodate and interact with pollutant molecules when they were entrapped on the aerogels (Fig. 8(b)). Figure 8(c) displays the dependence of Q_e and porosity on the MCC-MnO_2 mass fraction. The Q_e value increases gradually when the MCC-MnO_2 mass fraction is less than 20%, although the porosity decreases. The phenomenon can be ascribed to the fact that the adsorption of introduced MCC-MnO_2 particles has a greater effect than the slight decrease in porosity. As the MCC-MnO_2 mass fraction increases, the porosity declines rapidly, and the transmission of pollutants in aerogels is restricted, resulting in a small reduction of Q_e. Hence, porosity is a key factor, but not the only factor, determining the adsorption capacity of SA aerogels.

To further examine the cause of the adsorption capacity enhancement, an adsorption comparison of SA-based aerogels with equivalent amounts of MCC/MnO_2/MCC-MnO_2 is shown in Fig. 8(d). It is obviously that MnO_2 nanoparticles are the dominant factor to facilitate the adsorption capacity. The Q_e for Cu^{2+}, Pb^{2+}, congo red (CR) and MB is 1.48–1.88 times higher than that of neat SA aerogel, reaching values of 93.2 mg/g, 207.3 mg/g, 118.2 mg/g and 328.1 mg/g, respectively. This excellent adsorption performance can be attributed to two factors: the well-organized porous structures of SA areogels reconstructed by MCC-MnO_2 particles, and the functional groups (dominated by hydroxyl groups) and lamellae structures contributed by the massive birnessite MnO_2 nanoparticles.

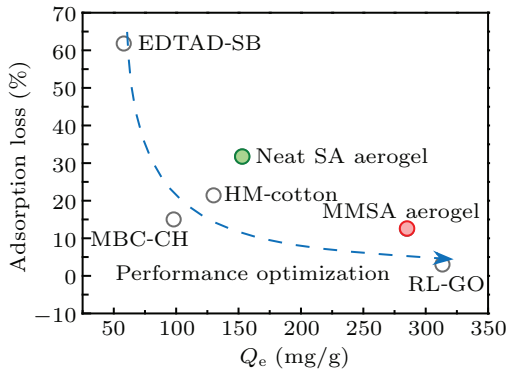


Fig. 9. Comparison of the MB adsorption performance of various materials. (EDTAD-SB: ethylenediaminetetraacetic dianhydride-modified sugarcane bagasse;[64] MBC-CH: modified ball clay and chitosan composite;[65] HM-cotton: hyperbranch-mesostructure functionalized cotton;[66] RL-GO: rhamnolipid-functionalized graphene oxide;[67] neat SA and MMSA aerogels are materials reported in this work).

As an effective adsorbent, the number of effective renewable cycles to recover the aerogels from the biosorbed pollutants is very crucial. As shown in Fig. 8(e), the adsorption capacity decreases slightly (only 13% of the initial adsorption amount is lost) even after 5 cycles. Compared with the reported adsorption materials in Fig. 9, the general performance of MMSA aerogels is very close to rhamnolipid-functionalized graphene oxide, but at much lower costs. Furthermore, neat SA aerogels collapse during application, while MMSA-20 aerogels maintain a shape that close to the initial state. Therefore, MMSA aerogels are cost-effective adsorbents with a high adsorption capacity and an outstanding regeneration performance.

3. Conclusion

This work demonstrates the principles and a strategy for reengineering the hierarchical structures of SA aerogels to enhance the macroscopic performance by meso-reconstruction. The multiscale materials of SA chains, the rod-like MCC and the MnO_2 nanoparticles were reassembled into a type of new aerogel that integrates the advantages of all the components. The MCC-MnO_2 particles were fabricated to control the organized dispersion of MnO_2 nanoparticles in aerogels. Via the templating function of MCC-MnO_2, the introduction of MCC-MnO_2 particles into SA sol provided more nucleation seeds and reduced the gelation time. Moreover, the reconstruction of the SA gel network was facilitated due to the short rod-like structure and the abundant hydroxyl groups of MCC-MnO_2 particles. These attributes enhanced the compressive strength and modulus, but the elasticity and deformation recovery were weakened to some extent. In general, the MMSA-20 aerogel can retain excellent elasticity and support 200 kPa of stress after five cyclic compression tests. The value of Q_e is 1.48–1.88 times higher than that of neat SA aerogel, reaching values of 93.2 mg/g, 207.3 mg/g, 118.2 mg/g and 328.1 mg/g for Cu^{2+}, Pb^{2+}, CR and MB, respectively. After 5 regeneration cycles, the aerogel shape remained intact, and the adsorption amount decreased slightly, indicating a renewable adsorbent suitable for the removal of metal ions (i.e., Cu^{2+} and Pb^{2+}) and dyes (i.e., CR and MB) from aqueous solutions.

Appendix A: Experimental details

Materials Sodium alginate (SA, medium viscosity, $M =$ 250000 g/mol) was purchased from Sigma-Aldrich (Shanghai, China). Manganese (II) sulfate monohydrate ($MnSO_4{\cdot}H_2O$), $KMnO_4$, HNO_3, NaOH, microcrystalline cellulose (MCC, average particle size 20–80 μm, polymerization degree 215–240), $CaCO_3$, D-glucono-δ-lactone (GDL), ethanol absolute, $Cu(NO_3)_2{\cdot}3H_2O$, $Pb(NO_3)_2$, typical cationic dye methylene blue (MB) and anionic dye congo red (CR) were obtained from

Sinopharm Chemical Reagent (Suzhou, China). All reagents were analytically neat and without any treatment.

Preparation of MCC-MnO_2 As displayed in Fig. 2, MCC-MnO_2 was prepared by redox manipulation.[45] Typically, 3.26 g MCC was mixed with 45 mL of a 0.02 M $MnSO_4$ solution under continuous stirring at 25 °C to allow adequate infiltration of the MCC. Then, 30 mL of a 0.02 M $KMnO_4$ solution was added dropwise into the reaction system. After the mixture reacted for 6 h, the suspension turned brownish black, and the product was centrifuged and washed with deionized water. The MCC-MnO_2 particles were obtained after drying at 50 °C.

Fabrication of MMSA aerogels In a typical synthesis, 1.5 g SA was added to 100 mL deionized water and stirred vigorously for 3 h to obtain a uniform solution. Then, 0.3 g MCC-MnO_2 was added and stirred for 3 h to obtain a homogeneous mixture. Subsequently, a certain amount of $CaCO_3$ was allowed to disperse in the mixture, followed by the addition of GDL. Here, $CaCO_3$ and GDL were used as a gel promoter[68,69] ("GDL-driving-Ca^{2+}-release" process), and their molar ratio of 1:2 was set to optimize the neutralization reaction. The mixture was cast into molds, frozen at −50 °C and dried for 48 h under vacuum (less than 10 Pa). Then, the shaped MCC-MnO_2/SA (MMSA) aerogels with an MCC-MnO_2 content of 10% (w/w) were acquired (abbreviated as MMSA-20). Similarly, a series of MMSA-0, MMSA-10, MMSA-30, MMSA-40 and MMSA-50 aerogels were fabricated according to the same procedure.

Structural characterization The surface morphologies of MCC-MnO_2 and MMSA aerogels were studied by field emission SEM (FE-SEM, S-4800, Hitachi, Japan). The crystal structures were determined using XRD (Bruker AXS, D8 Advance, USA). The rheological evolution was monitored by a rheometer (Bohlin Gemini HR Nano, Malvern Instrument, UK). FTIR (Nicolet 5700, Thermo Nicolet, USA) spectroscopy and x-ray photoelectron spectroscopy (XPS, Axis Ultra HAS, Shimadzu/Kratos, Japan) were recorded to identify the structures and chemical compositions. The size and morphology of MCC-MnO_2 were observed by FETEM (G2 F20 S-Twin, USA). The compressive strength was evaluated via a universal testing machine (Instron-3365, Instron, USA) at a compression rate of 1 mm/min.

Density and porosity of MMSA aerogels The density and porosity of MMSA aerogels were measured by liquid displacement.[70] Ethanol (density ρ_e) was used as the displacement liquid, and the test was conducted at 30 °C. An aerogel sample of weight W_0 was immersed into a graduated cylinder containing a known volume (V_1) of ethanol, and the air bubbles in the aerogel pores were evacuated under vacuum and replaced with ethanol until the pores were full; this volume was recorded as V_2. Then, the ethanol-impregnated aerogel was removed from the cylinder, and the residual ethanol volume was recorded as V_3. Therefore, the volume differences $(V_2 - V_1)$ and $(V_1 - V_3)$ were the volumes of the skeleton and the pores of the aerogel, respectively. Thus, the total volume of the aerogel was $V = (V_2 - V_1) + (V_1 - V_3) = V_2 - V_3$. The density of the aerogel (d) was expressed as

$$d = \frac{W_0}{V_2 - V_3}, \tag{4}$$

and the porosity (P) of the aerogel was determined by

$$P(\%) = \frac{V_1 - V_3}{V_2 - V_3}. \tag{5}$$

Adsorption and desorption experiments The aerogel (0.1 g) was added to 100 mL of different effluents with 500 mg/L of metal ions or dyes, and an adsorption experiment was carried out at 30 °C for 12 h to ensure saturated adsorption. For dyes, the supernatant was removed after adsorption for analysis with a UV-vis spectrophotometer (U-3010, Hitachi, Japan) by monitoring the absorbance changes at the maximum wavelength (664 nm and 497 nm for MB and CR, respectively). Instead of using UV-vis spectrophotometry, the concentrations of metal ion solutions were detected using inductively coupled plasma atomic emission spectroscopy (ICP-AES, iCAP 6000 DUO, Thermo Scientific, USA). The equilibrium adsorption capacity (Q_e) was calculated according to

$$Q_e = \frac{(C_o - C_e)V}{m}, \tag{6}$$

where C_o and C_e (mg/L) are the adsorbate concentrations at the initial and equilibrium time, respectively. V (L) denotes the volume of the pollutant solution, and m (g) is the mass of adsorbent used for the adsorption experiments.

To determine the reusability of MMSA aerogels, consecutive adsorption and desorption cycles were repeated five times by regeneration at 30 °C for 4 h. Specifically, for MMSA aerogels loaded with metal ions/MB, the eluent was 0.05 M HNO_3. Additionally, 0.05 M NaOH was used for MMSA-CR. After thorough washing, the aerogels were reassembled, freeze-dried and reemployed for wastewater treatment.

Acknowledgements

Project supported by the National Natural Science Foundation of China (Grant No. 12074322), Shenzhen Science and Technology Plan Project (Grant No. JCYJ20180504170208402), Science and Technology Project of Xiamen City (Grant No. 3502Z20183012), Science and Technology Planning Project of Guangdong Province, China (Grant No. 2018B030331001).

References

[1] Zhao S, Li Y, Yin H, Liu Z, Luan E, Zhao F, Tang Z and Liu S 2015 *Sci. Adv.* **1** e1500372
[2] Miller J S, Stevens K R, Yang M T, Baker B M, Nguyen D H T, Cohen D M, Toro E, Chen A A, Galie P A and Yu X 2012 *Nat. Mater.* **11** 768

[3] Davis M E 2002 *Nature* **417** 813
[4] Alsbaiee A, Smith B J, Xiao L, Ling Y, Helbling D E and Dichtel W R 2016 *Nature* **529** 190
[5] Horike S, Shimomura S and Kitagawa S 2009 *Nat. Chem.* **1** 695
[6] Ulker Z and Erkey C 2014 *RSC Adv.* **4** 62362
[7] Shi C, Hu F, Wu R, Xu Z, Shao G, Yu R and Liu X Y 2021 *Adv. Mater.* **33** 2005910
[8] Zhang Y, Chen C, Qiu Y, Ma L, Qiu W, Yu R, Yu W and Liu X Y 2021 *Adv. Funct. Mater.* **31** 2100150
[9] Krieg E, Weissman H, Shirman E, Shimoni E and Rybtchinski B 2011 *Nat. Nanotech.* **6** 141
[10] Yamaguchi A, Uejo F, Yoda T, Uchida T, Tanamura Y, Yamashita T and Teramae N 2004 *Nat. Mater.* **3** 337
[11] Yoo S, Kim J H, Shin M, Park H, Kim J H, Lee S Y and Park S 2015 *Sci. Adv.* **1** e1500101
[12] Zhao S, Zhang Z, Sèbe G, Wu R, Rivera Virtudazo R V, Tingaut P and Koebel M M 2015 *Adv. Funct. Mater.* **25** 2326
[13] Bai H, Chen Y, Delattre B, Tomsia A P and Ritchie R O 2015 *Sci. Adv.* **1** e1500849
[14] Qiu W, Patil, Hu F and Liu X Y 2019 *Small* **15** 1903948
[15] Chen Z, Hu F, Lin Z, Hu J, Shen R, Lin Y and Liu X Y 2021 *Small Sci.* **1** 2000049
[16] Wang X, Qiu W and Liu X Y 2023 *J. Crystal Growth* **603** 126977
[17] Song Y, Lin Z, Kong L, Xing Y, Lin N, Zhang Z, Chen B H and Liu X Y 2017 *Adv. Funct. Mater.* **27** 1700628
[18] Xing Y, Shi C, Zhao J, Qiu W, Lin N, Wang J, Yan X B, Yu W D and Liu X Y 2017 *Small* **13** 1702390
[19] Chen Z, Zhang H, Lin Z, Lin Y, Van Esch J H and Liu X Y 2016 *Adv. Funct. Mater.* **26** 8978
[20] Chen W, Li S, Chen C and Yan L 2011 *Adv. Mater.* **23** 5679
[21] Tran Diana N H, Kabiri S, Wang L S and Losic D 2015 *J. Mater. Chem. A* **3** 6844
[22] Yu R, Shi Y, Yang D, Liu Y, Qu J and Zhong Z Y 2017 *ACS Appl. Mater. Interfaces* **9** 21809
[23] McKee J R, Appel E A, Seitsonen J, Kontturi E, Scherman O A and Ikkala O 2014 *Adv. Funct. Mater.* **24** 2706
[24] Partap S, Rehman I, Jones J R and Darr J A 2006 *Adv. Mater.* **18** 501
[25] Lee K Y and Mooney D J 2012 *Prog. Polym. Sci.* **37** 106
[26] Wang L, Shelton R M, Cooper P R, Lawson M, Triffitt J T and Barralet J E 2003 *Biomaterials* **24** 3475
[27] Fan J, Shi Z, Lian M, Li H and Yin J 2013 *J. Mater. Chem. A* **1** 7433
[28] Jiao C, Xiong J, Tao J, Xu S, Zhang D, Lin H and Chen Y 2016 *Int. J. Biol. Macromol.* **83** 133
[29] Sone H, Fugetsu B and Tanaka S 2009 *J. Hazard. Mater.* **162** 423
[30] Balakrishnan B, Joshi N, Jayakrishnan A and Banerjee R 2014 *Acta Biomaterialia* **10** 3650
[31] Kundu J, Shim J H, Jang J, Kim S W and Cho D W 2015 *J. Tissue Eng. Regen. Med.* **9** 1286
[32] Balakrishnan B, Mohanty M, Umashankar P R and Jayakrishnan A 2005 *Biomaterials* **26** 6335
[33] Shamshina J, Gurau G, Block L, Hansen L, Dingee C, Walters A and Rogers R 2014 *J. Mater. Chem. B* **2** 3924
[34] Zhao J, Zhao X, Guo B and Ma P X 2014 *Biomacromolecules* **15** 3246
[35] Couvreur P 2014 *Nat. Nanotech.* **9** 874
[36] Li J, Illeperuma W R K, Suo Z and Vlassak J J 2014 *ACS Macro Letters* **3** 520
[37] Sun J Y, Zhao X, Illeperuma W R, Chaudhuri O, Oh K H, Mooney D J, Vlassak J J and Suo Z 2012 *Nature* **489** 133
[38] Kuo C K and Ma P X 2001 *Biomaterials* **22** 511
[39] Xiong R, Zhang X, Tian D, Zhou Z and Lu C 2012 *Cellulose* **19** 1189
[40] Eichhorn S J, Dufresne A, Aranguren M, Marcovich N, Capadona J, Rowan S J, Weder C, Thielemans W, Roman M and Renneckar S 2010 *J. Mater. Sci.* **45** 1
[41] Zhang J, Cao Y, Feng J and Wu P 2012 *J. Phy. Chem. C* **116** 8063
[42] Teng S X, Wang S G, Gong W X, Liu X W and Gao B Y 2009 *J. Hazard. Mater.* **168** 1004
[43] Liu R, Liu H, Zhao X, Qu J and Zhang R 2010 *J. Hazard. Mater.* **176** 926
[44] Chacón-Patiño M L, Blanco-Tirado C, Hinestroza J P and Combariza M Y 2013 *Green Chem.* **15** 2920
[45] Jiao C, Tao J, Xiong J, Wang X, Zhang D, Lin H and Chen Y 2017 *Cellulose* **24** 2591
[46] Wu R, Ma L and Liu X Y 2022 *Adv. Sci.* **9** 2103981
[47] Ma L, Liu Q, Wu R, Meng Z, Patil A, Yu R, Yang Y, Zhu S, Fan X, Hou C, Li Y, Qiu W, Huang L, Wang J, Lin N, Wan Y, Hu J and Liu X Y 2020 *Small* **16** 2000203
[48] Zhang L, Hu F, Zhu S, Lin Y, Meng Z, Yu R and Liu X Y 2020 *Small* **16** 2000128
[49] Chen X, Shao Z, Knight D P and Vollrath F 2007 *Proteins* **68** 223
[50] Qiu W and Liu X Y 2022 *Adv. Fiber Mater.* **4** 390
[51] Yu G, Hu L, Vosgueritchian M, Wang H, Xie X, McDonough J R, Cui X, Cui Y and Bao Z 2011 *Nano Lett.* **11** 2905
[52] Liang S, Teng F, Bulgan G, Zong R and Zhu Y 2008 *J. Phy. Chem. C* **112** 5307
[53] Chen H, He J, Zhang C and He H 2007 *J. Phy. Chem. C* **111** 18033
[54] Avramov I 2007 *Physica A* **379** 615
[55] Teh J W, Blom H P and Rudin A 1994 *Polymer* **35** 1680
[56] Rogers M A and Marangoni A G 2008 *Cryst. Growth Des.* **8** 4596
[57] Mallia V A, Terech P and Weiss R G 2011 *J. Phy. Chem. B* **115** 12401
[58] Shi C, Wang J, Sushko M L, Qiu W, Yan X and Liu X Y 2019 *Adv. Funct. Mater.* **29** 1904777
[59] Chen N, Wan C, Zhang Y and Zhang Y 2004 *Polymer Testing* **23** 169
[60] Xie X L, Liu Q X, Li R K Y, Zhou X P, Zhang Q X, Yu Z Z and Mai Y W 2004 *Polymer* **45** 6665
[61] Basrur V R, Guo J, Wang C and Raghavan S R 2013 *ACS Appl. Mater. Interfaces* **5** 262
[62] Nguyen A T, Huang Q L, Yang Z, Lin N, Xu G and Liu X Y 2015 *Small* **11** 1039
[63] Liu F, Chung S, Oh G and Seo T S 2012 *ACS Appl. Mater. Interfaces* **4** 922
[64] Xing Y, Liu D and Zhang L P 2010 *Desalination* **259** 187
[65] Auta M and Hameed B H 2014 *Chem. Eng. J.* **237** 352
[66] Tao J, Xiong J, Jiao C, Zhang D, Lin H and Chen Y 2017 *Carbohydr. Polym.* **166** 271
[67] Wu Z, Zhong H, Yuan X, Wang H, Wang L, Chen X, Zeng G and Wu Y 2014 *Water Res.* **67** 330
[68] Huang H, Lü S, Zhang X and Shao Z 2012 *Soft Matt.* **8** 4609
[69] Bigi A, Cojazzi G, Panzavolta S, Rubini K and Roveri N 2001 *Biomaterials* **22** 763
[70] Hsu Y Y, Gresser J D, Trantolo D J, Lyons C M, Gangadharam P R J and Wise D L 1997 *J. Biomed. Mater. Res.* **35** 107